symmetry

MDPI

Review

Moving Mesh Partial Differential Equation Modelling of a 5CB Nematic Liquid Crystal Confined in Symmetric and Asymmetric Pi-Cells: A Review

Antonino Amoddeo

Department of Civil, Energy, Environment and Materials Engineering, University 'Mediterranea' of Reggio Calabria, Via R. Zehender 1, Feo di Vito, I-89122 Reggio Calabria, Italy; antonino.amoddeo@unirc.it; Tel.: +39-0965-169-3299; Fax: +39-0965-169-22201

Abstract: The switching properties of nematic liquid crystals under electrical and mechanical stresses play a fundamental role in the design and fabrication of electro-optical devices. Depending on the stress applied to a nematic texture confined in a pi-cell, different nematic configurations are allowed inside the cell, while the induced distortion is relaxed by means of growing biaxial domains which can end with the order reconstruction phenomenon, a transition connecting two topologically different nematic textures which can occur in different regions of the pi-cell. Due to the different space and time scales involved, modelling in the frame of the Landau–de Gennes order tensor theory is mandatory to correctly describe the fast-switching mechanisms involved, while from a computational point of view, sophisticated numerical techniques are required to grasp tiny and fast features which can be predicted by the mathematical modelling. In this paper, we review the results obtained from the mathematical and numerical modelling of a 5CB liquid crystal confined in a pi-cell performed by using a numerical technique based on the equidistribution principle, tailored for the description of a complex physical system in which fast switching phenomena are coupled with strong distortions. After a recap on the underneath theory and on the numerical method, we focus on the switching properties of the nematic material when subjected to variable mechanical and electrical stresses in both symmetric and asymmetric conditions.

Keywords: mathematical modelling; equidistribution; MMPDE; biaxiality; order reconstruction

Academic Editor: Constantin Fetecau

Received: 17 November 2024
Revised: 21 December 2024
Accepted: 23 December 2024
Published: 27 December 2024

Citation: Amoddeo, A. Moving Mesh Partial Differential Equation Modelling of a 5CB Nematic Liquid Crystal Confined in Symmetric and Asymmetric Pi-Cells: A Review. *Symmetry* **2025**, *17*, 30. https://doi.org/10.3390/sym17010030

1. Introduction

Nematic liquid crystals (NLCs) play a crucial role in several technological applications regarding, but not restricted to, biophysics, materials design, and nanoscience, but above all, they are the key components for liquid crystal displays (LCDs) manufacturing, for which the ever-growing request for high performance sustains growing research efforts [1–3].

The recent discovery of ferroelectric NLCs opens the door, among other possible uses, to applications in tunable non-linear devices and efficient second-harmonic generation, while the photonic quantum technologies could benefit from their use as sources of quantum light [4].

Moreover, NLCs have been recently used to fabricate interactive liquid crystal fiber arrays for applications in soft robotics in the field of human–machine interactions [5].

In such context, mathematical modelling is a fundamental tool to understand phenomena observed when NLCs are subjected to mechanical and electrical stresses, as it happens when nematic molecules are confined within the so-called pi-cell [6,7]. The latter constitutes

the experimental set up appropriate to investigate the switching properties of NLCs and consists of two parallel flat glass plates, separated by spherical spacers with thickness in the micrometer range, where the nematic material is placed with a proper treatment of the cell for electrical connectivity and sealing. Anchoring is understood as the result of the interaction of a liquid crystal molecule with a confining glass plate, inducing its orientation along a given direction [3,8], while the anchoring angle of the nematic molecules on the two confining plates can be imposed by a proper treatment of the internal surfaces of the plates [6]. Very recently, the orientational and anchoring properties of a 5CB NLC interacting with a graphene oxide (GO) substrate have been investigated, evidencing GO inducing a planar alignment of the NLC molecules on the confining surfaces with strong anchoring energy, potentially allowing improvement in the design and manufacturing of optoelectronics devices [9].

NLCs are elongated molecules having a rod-like shape, and from a continuum point of view, constitute a system made of rods possessing five degrees of freedom, so their dynamical evolution is fully described by five independent parameters in the frame of the order tensor $\boldsymbol{Q}$ according to the Landau–de Gennes theory [10,11]. When the NLC is subjected to small elastic distortions, its response can be described within the classical Oseen–Frank theory [12,13], in terms of director and scalar order parameter. The first is a unit vector, $\boldsymbol{n}$, accounting for the average orientation of the molecular long axis of the nematic molecule, while the degree of order along such direction is accounted for by the scalar order parameter S. In the presence of a suitable electric field, a nematic molecule reorients its molecular long axis along the field direction; and so behaves the director $\boldsymbol{n}$, while removing the electric field, the nematic turns back to its initial configuration; such a situation is what happens in the Freedericksz transition [14], for the elastic distortion of an NLC confined between plates. In this case, the nematic is said to be uniaxial as it possesses a unique optical axis identified by the director, and the NLC has a monostable behaviour, a well-known phenomenon exploited in LC devices [15].

NLCs exhibit multistable behaviours that manifest themselves in a variety of situations which can be useful for designing electro-optical devices with advanced performances involving memory effects [16]. Biaxiality is a property of NLCs which cannot be explained in the frame of the classical theory, requiring, instead, a description within the Landau–de Gennes order tensor theory, as when the elastic distortions occur within a length-scale which is comparable to the biaxial coherence length ξ_b [10,14]. While uniaxial NLCs have a unique optical axis and cylindrical symmetry around the director, biaxial nematics possess two distinct optical axes, as the above symmetry is broken, a condition deserving in-depth attention regarding the implications it could have, for example, in improving LCDs technology.

Among the wealth of studies that have investigated biaxial phenomena in recent decades, we recall here some of particular interest, such as those of Schopohl and Sluckin [17], and Buscaglia et al. [18], for their investigation on topological defects in NLCs, as well as the review of Kleman and Lavrentovich [19]. The behaviour of NLCs confined in porous matrices has been investigated by Aliev and Basu [20], NLC droplets dispersed in the aqueous phase have been studied by Tjipto et al. [21], while Yi et al. [22] evidenced as the NLC director undergoes a transition from planar to homeotropic under the effect of a topographical pattern. Self-organized colloidal dispersions have been studied by Loudet et al. [23], Smalyukh et al. [24], and by Musevic et al. [25].

High degrees of frustration can be induced in nematic textures subjected to mechanical and electric stresses, and the growth of biaxiality inside uniaxial NLCs is a way of relaxing such distortions. Electric fields applied to NLCs have been used to induce biaxial domains in several conditions. Quian [26] observed a competition between the NLC order and the

electric field inducing a biaxial region in which the order varies close to the surface where the nematic is subjected to strong anchoring, a condition which is equivalent to 'infinite' anchoring energy [27]. The effect of a strong electric field applied to an NLC has been investigated by Martinot-Lagarde et al. [28], who found that a transient melted biaxial state connects in the bulk textures with different orders; Ambrozic et al. [29] studied the biaxial structure of a defect core under the action of an external electric field, while Biscari et al. [30] explored the biaxiality of the order tensor when enforcing homeotropic anchoring conditions of the NLC on a curved surface.

The biaxial order reconstruction (OR) phenomenon is a mechanism that connects two topologically different nematic textures through a wealth of biaxial states without director rotation, mathematically interpreted within the eigenvalues exchange mechanism of the Landau–de Gennes $\boldsymbol{Q}$ tensor theory, leading the way to the design of bistable/multistable electro-optical devices [31,32]. In ref. [6], the experimental evidence of the OR phenomenon in an NLC with symmetric anchoring conditions is analyzed and interpreted via a mathematical model, and further experimental investigations of OR occurring in the bulk of an NLC have been characterized through measurements of the electric current flowing across the cell, distinguishing among different contributions [33–35]. In [36,37], the influence of dopants on the transient biaxial order, and hence on the OR electrically induced in a thermotropic calamitic nematic has been investigated, as well as inhomogeneous OR driven by modulation in the anchoring conditions of the nematic [38]; Carbone et al. [39] measured the force between an atomically flat mica sheet and a micrometer-sized glass sphere immersed in an NLC using atomic force microscopy, observing a structural transition of the NLC when the separation between the mica sheet and the glass sphere is below a critical value, thus relaxing the elastic distortion through biaxial transitions interpreted in the context of the eigenvalues exchange of the order tensor.

The nematic OR in an NLC has been studied also in pi-cells with asymmetric anchoring conditions, demonstrating that OR close to a boundary surface with strong anchoring conditions is equivalent to anchoring breaking [40], while for electric fields below, but close to, the threshold for the biaxial OR, the biaxial order spreads on the surface [27]. Experiments aimed at distinguishing bulk and surface OR phenomena have been recently performed, but no resolutive results have been obtained up to now [41,42].

Kralj and Majumdar [43] numerically investigated static effects on the OR pattern for an NLC confined in shallow sub-micrometer scale wells with square cross sections, finding a new two-dimensional star-like biaxial order reconstruction pattern; Zhou et al. [44] modelled the OR transitions of an NLC confined between two coaxial cylinders as a function of their separation; Sun et al. [45] studied the OR in an inverse twisted nematic liquid crystal cell under the action of an electric field in two spatial dimensions, framed within the eigenvalues exchange in the Landau–de Gennes theory.

The biaxial phenomena under consideration are characterized by fast order switching occurring over length scales comparable with $\xi_b \approx 10$ nm [46], which modelling within the Landau–de Gennes $\boldsymbol{Q}$ tensor theory results in a system of five coupled, non-linear partial differential equations (PDEs), one for each of the degrees of freedom of the rod-like nematic molecules. A further PDE considers the coupling of the above model equations with the applied electric field, providing the electrical stress capable of reorienting the nematic director. The six coupled non-linear PDEs can be solved numerically to obtain the dynamical evolution of the system, but, given the strong anisotropies resulting from the fast switching phenomena arising, the need for effective computational techniques to improve the numerical resolution and to grasp finer details has emerged. For this purpose, the moving mesh PDE (MMPDE) numerical technique has been implemented with the finite

element method (FEM) [47–49], a method allowing us to improve the numerical resolution while minimizing the computational effort.

The technique was applied for the first time to the numerical investigation of NLCs by Ramage and Newton [49,50], testing the experimental and numerical results presented in [6]. Afterwards, other papers focused on improving the mathematical and numerical modelling of the switching properties of NLCs using the same technique, both in one- and two-spatial dimensions [51–53]. In the past years, from a more applicative perspective, the MMPDE technique has been applied to the study of the biaxial properties of a 5CB NLC confined in a pi-cell, modelled with both symmetric and asymmetric anchoring angles, imposing different mechanical and electrical stresses [8,54–60]. This review, therefore, explores the emergence of effects due to the application of different stresses in a unified vision across several numerical experiments, highlighted together with the numerical technique after a summary of the basic theory.

2. Theoretical Overview

The mathematical modelling of the NLCs dynamics is tackled by variational principles, minimizing a free energy functional F, which, in the Landau–de Gennes theory, is a function of the order tensor $\boldsymbol{Q}$ and of its gradient. The order tensor $\boldsymbol{Q}$ is second rank, symmetric, and traceless, expressed in the orthonormal basis of its eigenvectors $\boldsymbol{u}_i$,

$$\boldsymbol{Q} = \sum_{i=1}^{3} \lambda_i \boldsymbol{u}_i \otimes \boldsymbol{u}_i, \tag{1}$$

hence, the eigenvalues λ_i fulfill the condition $\lambda_1 + \lambda_2 + \lambda_3 = 0$. The eigenvectors point in the direction of the axes of the reference frame, while each eigenvalue gives the degree of the nematic order along the direction of the associated eigenvector. Nematic molecules can be arranged in an isotropic phase in which they are completely disordered without positional or orientational order, behaving, from an optical point of view, as an isotropic liquid: in this phase, all three eigenvalues are equal and $\boldsymbol{Q} = \boldsymbol{0}$. If the molecules are in the uniaxial phase, the optical axis is identified by the eigenvector associated with the maximum eigenvalue, $\lambda_i = \lambda_{\max}$, which identifies the director, then $\boldsymbol{u}_i = \boldsymbol{n}$; the other eigenvalues have equal values, and the scalar order parameter is $S = (3/2)\,\lambda_{\max}$. When the nematic molecules are in the biaxial phase, the three eigenvectors have different, nonzero values, then the LC phase can be correctly described within the $\boldsymbol{Q}$ tensor theory, as biaxial domains are not considered as mathematical singularities, and the order is a function of the local coordinates [61]. Moreover, the invariant measure of the biaxiality gives the degree of the induced biaxial order [6,40],

$$\beta = \sqrt{1 - 6\frac{\mathrm{tr}\left(\boldsymbol{Q}^3\right)^2}{\mathrm{tr}\left(\boldsymbol{Q}^2\right)^3}} \quad \in [0,1], \tag{2}$$

where $\beta = 0$ means that the LC is in a uniaxial state, while $\beta = 1$ when the nematic texture is in a biaxial phase.

Since the NLC has five degrees of freedom, the order tensor can be expressed in terms of five independent parameters as

$$\boldsymbol{Q} = \begin{pmatrix} q_1 & q_2 & q_3 \\ q_2 & q_4 & q_5 \\ q_3 & q_5 & -q_1 - q_4 \end{pmatrix} \tag{3}$$

where $q_i = q_i(\boldsymbol{x}, t)$, $\boldsymbol{x}$ being the spatial coordinate and t the time.

The free energy F of the LC includes bulk and surface contributions [40]:

$$F = F_b + F_s \tag{4}$$

Considering the NLC confined in pi-cells with strong anchoring conditions on the boundary plates, hence, with infinite anchoring strength, the surface contribution to the free energy is fixed and can be neglected. Then, the free energy for the confined nematic can be written as [10]

$$F = \int_V (f_t + f_d + f_e) dV. \tag{5}$$

In the above equation, f_t, f_d, and f_e are thermotropic, elastic, and electric free energy densities, respectively, the last one coming from the application of an external electric field, and are functionals according to

$$f_t = f_t(\boldsymbol{Q}), f_d = f_d(\boldsymbol{Q}, \nabla \boldsymbol{Q}), f_e = f_e(\boldsymbol{Q}, \nabla \boldsymbol{Q}). \tag{6}$$

Recalling some definitions as, for example, in refs. [6,40], at a temperature T, if T^* is the supercooling temperature at which the isotropic phase becomes unstable, and α_t is a positive constant, then $a = \alpha_t (T - T^*) = \alpha_t \Delta T$. The equilibrium order parameter for uniaxial systems is defined as

$$S_{eq}(\Delta T) = \frac{b}{4c}\left(1 + \sqrt{1 - \frac{24ac}{b^2}}\right), \tag{7}$$

where b and c are in turn set as constants. Introducing the Frank elastic constants k_{11}, k_{22}, and k_{33}, then

$$L_1 = \frac{k_{33} - k_{11} + 3k_{22}}{6S_{eq}^2}, \; L_2 = \frac{k_{11} - k_{22}}{S_{eq}^2}, \; L_6 = \frac{k_{33} - k_{11}}{2S_{eq}^3}. \tag{8}$$

If ε_0 is the vacuum dielectric constant, while $\varepsilon_{\parallel}$ and $\varepsilon_{\perp}$ are, respectively, the nematic dielectric constants which are parallel and perpendicular to the nematic axis, the isotropic and the anisotropic dielectric susceptibilities, ε_i and ε_a, can be written as

$$\varepsilon_i = \frac{\varepsilon_{\parallel} + 2\varepsilon_{\perp}}{3}, \; \varepsilon_a = \frac{\varepsilon_{\parallel} - \varepsilon_{\perp}}{S_{eq}}. \tag{9}$$

Finally, admitting that the free energy densities depend on small $\boldsymbol{Q}$ distortions, the expansion in powers of $\boldsymbol{Q}$ gives

$$f_t = a\mathrm{tr}\boldsymbol{Q}^2 - \frac{2b}{3}\mathrm{tr}\boldsymbol{Q}^3 + \frac{c}{2}\left(\mathrm{tr}\boldsymbol{Q}^2\right)^2, \tag{10}$$

$$f_d = \frac{L_1}{2}\left(\frac{\partial Q_{ij}}{\partial x_j}\right)^2 + \frac{L_2}{2}\frac{\partial Q_{ij}}{\partial x_j}\frac{\partial Q_{ik}}{\partial x_k} + \frac{L_6}{2}Q_{lk}\frac{\partial Q_{ij}}{\partial x_l}\frac{\partial Q_{ij}}{\partial x_k}, \tag{11}$$

$$f_e = \frac{\varepsilon_0}{2}\left(\varepsilon_i |\nabla U|^2 + \varepsilon_a \nabla U \cdot \boldsymbol{Q} \nabla U\right) + \bar{e} \nabla Q \cdot \nabla U. \tag{12}$$

In Equation (12), U is an appropriate electric potential applied to the pi-cell, while the last term accounts for polarization effects with $\bar{e}$ flexoelectric parameter.

The evolution of each $q_i = q_i(\boldsymbol{x}, t)$ in Equation (3) is obtained from the balance of the energy variation

$$\delta \mathfrak{D} + \delta \dot{F} = 0, \tag{13}$$

where

$$\mathfrak{D} = \int_V \mathcal{D} dV = \int_V \gamma \mathrm{tr}\dot{\boldsymbol{Q}}^2 dV, \tag{14}$$

in which $\mathcal{D}$ represents the Rayleigh dissipation function and γ is a viscosity coefficient [6,40]. Inserting Equations (10)–(12) and (14) in Equation (13), five generalized Euler–Lagrange equations for each of the q_i are obtained,

$$\frac{\partial \mathcal{D}}{\partial \dot{q}_i} + \frac{\partial f_t}{\partial q_i} + \frac{\partial f_e}{\partial q_i} + \frac{\partial f_d}{\partial q_i} - \frac{\partial}{\partial x_j}\left(\frac{\partial f_d}{\partial q_{i,j}}\right) - \frac{\partial}{\partial x_j}\left(\frac{\partial f_e}{\partial q_{i,j}}\right) = 0, \quad i = 1, \ldots 5, \tag{15}$$

where 'j' means differentiation with respect to the spatial coordinates.

The dynamical evolution of the order tensor is obtained by solving the PDE system constituted by Equations (15) together with the governing equation for the electric potential in the absence of free charges

$$\nabla \cdot \boldsymbol{D} = \nabla \cdot [-\varepsilon_0(\varepsilon_i \boldsymbol{I} + \varepsilon_a \boldsymbol{Q})\nabla U + \bar{e}(\nabla \cdot \boldsymbol{Q})] = 0. \tag{16}$$

In the last equation, the first term in round brackets is the dielectric tensor, while the second one is the spontaneous polarization vector balancing the effect of the electric potential.

3. Numerical Method

The mathematical modelling of the above physical problem leads to a system of six coupled, non-linear PDEs to be solved numerically. On the other hand, a reliable and efficient computational method, capable of ensuring a numerical resolution adequate to grasp fast and tiny variations in the biaxial order is desirable. The numerical solution of PDEs using the FEM is based on an appropriate discretization of the integration domain, which is divided in elements delimited by nodes, and the set of the elements constitutes the mesh. The approximate solution of the problem is computed on the nodes while inside each element the solution is interpolated by means of shape functions, usually of quadratic order. It turns out that the mesh quality plays a crucial role in the computational process: in general, denser meshes in domain regions where strong variations in the variables occur are capable of ensuring a better numerical resolution, but the computational cost becomes an issue. The question of the mesh quality has been tackled in different ways with the aim to obtain reliable solutions and robust computational methods [49,62–67], while the resolution requirement must be contempered with the minimization of the computational costs: with uniform discretizations, the resolution can be improved by increasing the number of nodes, hence building a denser mesh even in domain regions where high resolution is not required, for example, where there is a slow variation in the variables, resulting in a waste of computational resources. The use of adaptive methods, instead, allows us to concentrate the computational effort in the regions of the integration domain where it is most needed. Adaptive grid algorithms can be classified based on the strategy they adopt [62]: using h-methods, the mesh can be refined (or coarsened) by insertion (or elimination) of nodes, and in this case, improving the resolution means growing computational load; in p-methods, the order of the polynomial used to interpolate the solution inside the element is enriched, compatibly with the mesh roughness, in order to ensure stability and convergence of the solution. In r-methods, to which the MMPDE belongs, both the number of elements and nodes are kept constant, but the latter are clustered in regions of the integration domain where an improved resolution is required, and at the same time they are moved away from regions of low variability of the solution. Moreover, mixed h- and r-adaptive methods exist as, for example, in ref. [68]. The grid movement can be obtained by equidistributing a function, called the monitor function [69], over the integration domain. The appropriate monitor function retains the physical characteristics of the system under study; hence, its equidistribution allows us to obtain the mesh equation by which the nodes are moved across the domain according to the evolution of a well-identified physical property.

To implement the MMPDE numerical technique using the FEM in one space dimension (1D) based on the equidistribution principle [69–73], it is possible to proceed as follows.

Preliminarily, a physical domain Ω_p = [0, 1] spanned by the physical coordinate x, and a computational domain Ω_c = [0, 1] spanned by the computational coordinate ξ are defined.

If T is a time interval, a mapping of the physical space $\Omega_p \times T$ into the computational space $\Omega_c \times T$ is expressed by means of a coordinate transformation [8,49,70]:

$$\xi = \xi\,(x, t),\ x \in \Omega_p,\ t \in (0, T], \tag{17}$$

or, in reverse,

$$x = x\,(\xi, t),\ \xi \in \Omega_c,\ t \in (0, T]. \tag{18}$$

Then, $N + 1$ equispaced points in the 1D computational space Ω_c, $\xi_i = i/N$, $i = 0, 1, 2, \ldots, N$ correspond to a grid in the physical space $x_0(t) < x_1(t) < \ldots x_N(t)$, where $x_0(t) = 0$, and $x_N(t) = 1$.

A function $\rho(x, t)$ continuous over the interval [0, 1] is equidistributed if, given a constant c, it satisfies [8,49,69,70,74–77]

$$\int_{x_i(t)}^{x_{i+1}(t)} \rho(x,t)dx = c,\ \forall i = 0, 1, \ldots N. \tag{19}$$

Hence, for $i = 0, 1, \ldots N$,

$$\int_0^{x_i(t)} \rho(x,t)dx = \int_0^{x_1(t)} \rho(x,t)dx + \cdots + \int_{x_{i-1}(t)}^{x_i(t)} \rho(x,t)dx = c + \cdots + c = ic. \tag{20}$$

The constant c is determined from

$$\int_0^1 \rho(x,t)dx = \int_{x_0(t)}^{x_1(t)} \rho(x,t)dx + \int_{x_1(t)}^{x_2(t)} \rho(x,t)dx + \cdots + \int_{x_{N-1(t)}}^{x_N(t)} \rho(x,t)dx = c + \cdots + c = Nc, \tag{21}$$

giving

$$c = c(t) = \frac{1}{N}\int_0^1 \rho(x,t)dx. \tag{22}$$

Equation (20) now can be rewritten as

$$\int_0^{x_i(t)} \rho(x,t)dx = \frac{i}{N}\int_0^1 \rho(x,t)dx = \xi_i \int_0^1 \rho(x,t)dx,\ i = 0, 1, 2, \ldots, N, \tag{23}$$

where $\xi_i = i/N$ represents a uniform mesh on the computational space defined above. Considering the coordinate transformation $\Omega_c \times T \to \Omega_p \times T$, $x_i = x\,(\xi_i, t)$, then

$$\int_0^{x(\xi_i,t)} \rho(x,t)dx = \frac{i}{N}\int_0^1 \rho(x,t)dx = \xi_i \int_0^1 \rho(x,t)dx,\ \text{for } i = 0, 1, 2, \ldots, N. \tag{24}$$

In continuous form, it follows that

$$\int_0^{x(\xi,t)} \rho(x(\xi, t))dx = \xi \int_0^1 \rho(x(\xi), t)dx,\ \forall \xi = 0, 1, \ldots N. \tag{25}$$

Differentiating the previous equation with respect to the computational coordinate ξ, and making use of Equation (21) with $Nc = C(t)$, the mesh equation is obtained, giving, at each time step, the distribution of the mesh nodes inside the domain:

$$\rho(x(\xi, t))\frac{\partial}{\partial \xi}x(\xi, t) = \int_0^1 \rho(x(\xi), t)dx = C(t). \tag{26}$$

From Equation (26), it can be seen that, given a fixed number of mesh points, the function $\rho(x, t)$ must be small in regions where the variation of $x(\xi, t)$ is large, and vice versa. Up to now, nothing has been said about the function $\rho(x, t)$ which is called the mesh

density function or monitor function [69] (sometimes, this term is attributed to $\rho(x, t)^2$), for the reason that its equidistribution allows us to control the mesh points distribution in the physical domain. Since its choice has a key role for the optimal distribution of the mesh points over which a numerical solution is computed, a monitor function depending on the unknown solution $u(x, t)$ can be chosen. Hence, putting $\rho(x, t) = \mathrm{M}(u(x, t))$ allows the solution itself to control the mesh map quality and nodes distribution during the solution procedure, while other valid choices are based on solution error [69,75]. In practice, the functional expression of the monitor function depends on the nature of the problem to be solved, such as the steepness of the solution or its derivatives in particular regions of the physical domain.

The dynamical evolution of the biaxial order in an NLC which undergoes strong distortions is characterized by fast switching phenomena falling within the microsecond time interval. Moreover, they are confined to narrow spatial regions comparable to the electrical coherence length ξ_E, and in turn comparable to $\xi_b \approx 10$ nm [6,46], thus involving computations spanning over different length and time scales. It has been demonstrated [8] that, for 1D problems, a monitor function based on the solution gradient computed during the solution procedure, having the form proposed in [74] and called the Beckett-Mackenzie (BM) monitor function, is the most suitable for the description of the systems under consideration:

$$M(u(x,t)) = \alpha + \sqrt{\left|\frac{\partial u(x,t)}{\partial x}\right|}, \tag{27}$$

where

$$\alpha = \int_0^1 \sqrt{\left|\frac{\partial u(x,t)}{\partial x}\right|} dx. \tag{28}$$

α is a tuning parameter for the mesh adaptation, the task of which is to fix a floor for the clustering of the nodes inside the domain, and its determination is incorporated in the solution procedure and updated at each time step; please refer to [8] for details. In short, the mesh adaptivity is controlled by choosing a monitor function tightly related to the order variation, imposing in Equations (27) and (28) that

$$u(x,t) = tr(\boldsymbol{Q})^2. \tag{29}$$

In all reported cases, at $t = 0$, the nematic texture is in a splay configuration, and the director $\boldsymbol{n}$ is parallel to the boundary plates. The boundary conditions, instead, were prescribed case by case by the strong anchoring conditions. On the confining plates, Dirichlet boundary conditions were imposed for the order tensor, implying $\boldsymbol{Q} = \boldsymbol{Q}_s$, where $\boldsymbol{Q}_s$ is the order tensor on the boundary surfaces accounting for the pretilt angles. The imposed electric potential U also obeys to Dirichlet boundary conditions. Thus, at $t = 0$, the electric pulse amplitude is zero and the $\boldsymbol{Q}$ tensor represents a splayed nematic texture compatible with the imposed pretilt angles on the boundaries. The 1D integration domain corresponds to the thickness of a pi-cell 1mm thick, while the dynamical evolution is sampled in a time interval of up to 0.25 ms.

At each time step, the six coupled PDEs are solved simultaneously for each of the six unknown $u(x, t)$, according to the following multi-pass algorithm:

1. A uniform grid $x_j(0)$ is generated at $t = 0$, and the corresponding initial solution $u_j(0)$ is computed using the FEM.
   mesh and solution are updated in a temporal loop, putting forward the PDEs (15) and (16):
   while $t_n < T$
   the mesh is redistributed in a few steps $\nu \geq 0$:
   do
2. The monitor function is evaluated, and the grid is moved from $x_j(\nu)$ to $x_j(\nu + 1)$ with an iterative procedure equidistributing the monitor function in each subinterval, and a solution $u_j(\nu + 1)$ is calculated on the newly generated mesh.
   until $\nu \leq \nu_{max}$
3. The PDE system is put forward on the new mesh $x_j(\nu + 1)$ to obtain a numerical approximation $u_j(\nu + 1)$ at the new time level t_{n+1}.

end.

4. Numerical Results on Symmetric and Asymmetric Pi-Cell

In the following, we will go through some numerical experiments carried out on a 5CB NLC confined in a pi-cell with strong anchoring conditions and pretilt angles spanning various conditions, both symmetric and asymmetric, as will be specified case by case.

The pretilt angle is intended as the angle between the NLC molecular axis and the surface plane but directed in opposite directions on the boundary plates, as shown in Figure 1 for the symmetric case.

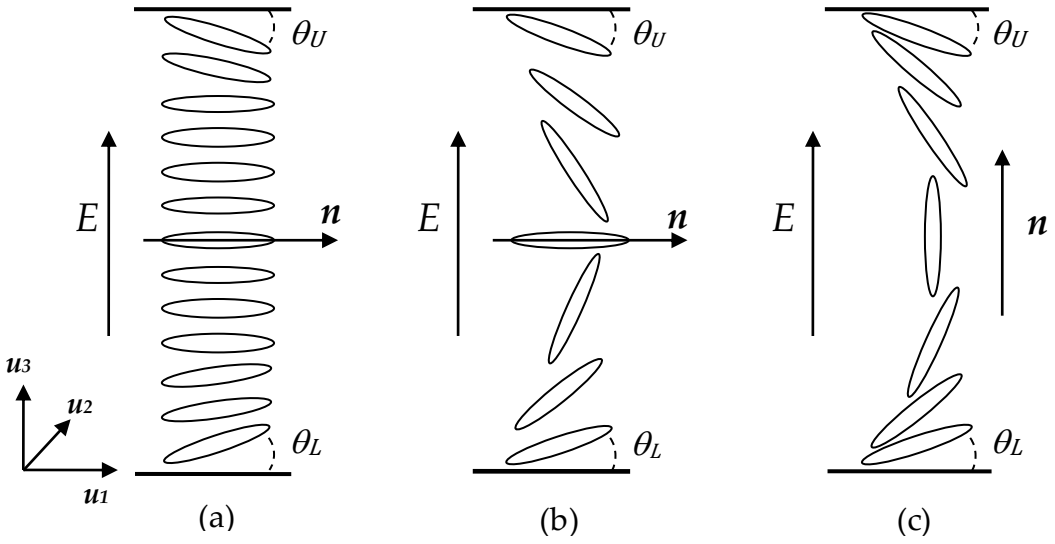

Figure 1. Geometry of the symmetric pi-cell with nematic molecules in different states, for generic pretilt angles $\theta_L = \theta_U$: (**a**) horizontal alignment with a slight splay; (**b**) intermediate state, with a thin horizontal wall in the center (OR); (**c**) mostly vertical alignment (pi-bent).

In practice, see, for example, ref. [8], these conditions permit, at equilibrium, the existence of two topologically different nematic textures: one in which the nematic molecules are mostly parallel to the confining plates, or slightly splayed, but on average the director is horizontal, see Figure 1a; the other, pi-bent, is like in Figure 1c, in which the molecules are aligned mostly vertically. The pretilt angles induce mechanical distortions to the nematic texture close to the confining plates, and in case of asymmetric pretilt angles, see Figure 2, such distortions grow close to the surface where the pretilt angle approaches the planar angle [27,46,56]. From a topological point of view, a pi-bent texture is equivalent to a pi-twisted one, i.e., textures starting from the splay configuration as in Figure 1a suffer a

180° torsion around the molecular axis instead of a 180° bending as in Figure 1c, see ref. [6]. A fast switching from a splay configuration to a pi-bent one is possible by the application of an electric field beyond a threshold necessary to overcome the energy barrier between the two configurations, and the two textures are connected by a biaxial transient state characterized by molecules remaining parallel to the plates without any director rotation. From a tensorial point of view, this corresponds to the exchange of two $\boldsymbol{Q}$ eigenvalues, i.e., to the OR phenomenon depicted in Figures 1b and 2b, for the symmetric and asymmetric cases, respectively.

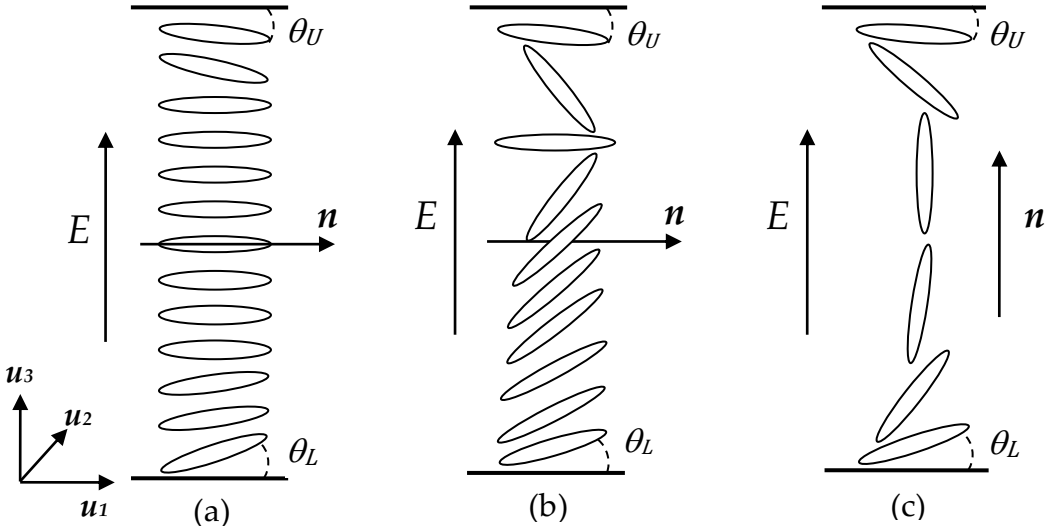

Figure 2. Geometry of the asymmetric pi-cell with nematic molecules in different states, for pretilt angles $\theta_L = 19°$ and $\theta_U = -3°$: (**a**) horizontal alignment with a slight splay; (**b**) intermediate state, with a thin horizontal wall (OR) close to the upper boundary plate; (**c**) mostly vertical alignment (pi-bent).

4.1. Symmetric Pi-Cell

Considering an NLC confined in a symmetric pi-cell subjected to mechanical and electric stresses, the former are induced by imposing appropriate pretilt angles to the nematic molecules, while the latter by the application to the confining plates of electric pulses with intensity suitable to induce the biaxial OR. In ref. [8] was simulated an experimental setup with pretilt angles on upper and lower bounding plates of, respectively, $\theta_U = -10°$ and $\theta_L = 10°$, both measured with respect to each plate, applying an electric pulse with amplitude $E = 11.4$ V/μm with duration $\tau = 0.25$ ms. The choice of the electric pulse amplitude corresponds to the threshold for the biaxial OR to occur, as determined in ref. [40].

The study [8] reports on three different MMPDE algorithms implementing three different monitor functions, but we focus only on the one containing BM as it has proven to be the most efficient, giving the more reliable results if compared with those reported in ref. [40], and clearly showed that the MMPDE method is capable of better resolving the dynamics inside the pi-cell. Such evidence results also from the inspection of the mesh trajectories, which show excellent adaptation to the order evolution inside the cell, according to the choice made with Equation (29), thus improving the quality of the numerical results. The algorithm implementing the BM monitor function concentrates the mesh points in regions of the integration domain where more resolution and accuracy is needed during the time evolution, i.e., in the cell center where the biaxial order reconstruction takes place, and at the cell boundaries where a certain mechanical stress is present due to the strong anchoring conditions and to the pretilt angle imposed. Nevertheless, in the bulk regions, as well, an adequate collocation of mesh points is guaranteed. Moreover, according to

the Landau–de Gennes theory, the biaxial OR is correctly framed in the context of the eigenvalues exchange and occurs after about 55 μs from the application of the electric pulse, a value which corresponds to the crossing time of two eigenvalues of the $\boldsymbol{Q}$ tensor, as reported in the paper.

Imposing electric stresses ranging from E = 10 V/μm to E = 14 V/μm with step ΔE = 1 V/μm, at fixed pretilt angles $\theta_U = -19°$ and $\theta_L = 19°$, thus increasing the mechanical distortion close to the boundary plates, the numerical results show that, already with an applied electric field E = 10 V/μm the biaxial OR occurs, then a lowering of the electric field threshold for OR occurs too because of the increased mechanical stress [55]. Moreover, increasing the electric pulse amplitude results in a progressively faster OR which moves from 38.5 μs to 17.5 μs, going from E = 10 V/μm to E = 14 V/μm, respectively (see Table 1). Such movement is also accurately predicted from the computation of the electric current flowing across the cell, as reported in the ref. [55]. Further, the competition between the applied electric field and the strong anchoring conditions induces a persistent biaxial wall close to the boundary plates, which grows with increasing electric field strength without undergoing relaxation by means of OR.

Table 1. Temporal position $\Delta\tau$ of the OR transition, occurring in the cell center as a function of the intensity of the applied electric pulse E, for symmetric pretilt angles as indicated.

	$\theta_{L/U}$ = +/−10°	$\theta_{L/U}$ = +/−19°										
E (V/μm)	11.4	10	11	12	13	14	18	20	32	40	60	90
$\Delta\tau$ (μs)	55	38.5	31	25	21	17.5	8	6	2	1	0.3	0.2

As long as the OR is slow, on the biaxiality maps, it is characterized by a uniaxial state surrounded by a biaxial ring having cylindrical symmetry but, as will be seen later, this will no longer be true for sufficiently intense applied electric fields.

In the presence of extreme electrical stresses, obtained by applying electrical pulses with increasing amplitudes from 18 V/μm to 90 V/μm [57], the predictions indicate that the OR relaxing the distortion of the nematic texture becomes ever faster: at E = 18 V/μm, it is located about 9 μs from the pulse start, and increasing the electric stress, the biaxiality grows consistently, with the OR starting to squeeze along the cell thickness. At E = 32 V/μm, the biaxiality is distributed along the cell thickness within about 3 μs from the pulse start, while the biaxial OR has definitively lost its cylindrical symmetry, but the splay to bend transition mediated by the OR is always correctly framed within the eigenvalues exchange mechanism predicted by the Landau–de Gennes theory. In Table 1 are summarized the temporal positions $\Delta\tau$ of the OR transition occurring after the pulse start, as a function of the pulse intensity, according to what was reported in [8,55,57]. The paper [57] reports also on the evolution of the eigenvalue associated with the eigenvector parallel to the electric field direction, and its monitoring indicates that the splay to bend transition can assume two different characteristics: below the boundary plates, and towards the cell center, the texture is in a uniaxial state and characterized as a first-order transition propagating towards the cell center with decreasing speed, while it becomes second order in correspondence of the biaxial OR in the cell center. The speed difference among transitions occurring near the cell center (slower) and transitions occurring towards the boundaries (faster) tends to vanish as the electric pulse amplitude increases to E = 60 V/μm, above which the transitions are always of the second order.

In summary, the studies reported in papers [8,55,57] predict that strong mechanical and electric stresses applied to an NLC confined in a symmetric pi-cell induce a growing biaxiality ending with the biaxial OR, which relaxes the induced distortion arising from the competition between two distinct mechanisms: from one side, the strong anchoring

condition forces the nematic close the boundary plates in a tilted configuration from which it cannot escape; on the other side, the electric field applied along the cell thickness forces the nematic to align parallel to the field direction, thus perpendicular to the plates, but either increasing the pretilt angle, or the intensity of the applied electric pulse, or both causes the speed increase in the biaxial OR that, due to the symmetry of the cell, occurs in the cell center. Also, the molecules that are close to the boundary plates are subjected to a growing biaxiality due to the even growing strain close to such a spatial region. The OR loses its cylindrical symmetry when high enough electric pulses cause its squeeze along the cell thickness; this implies that the core of the OR is not characterized by a single uniaxial state, but rather by a continuous succession of uniaxial states. In addition, the splay to bend transition of the nematic texture under the action of the electric field is of the second order and is located in the cell center, when it is accompanied by the biaxial OR, but is of the first order when the nematic order is uniaxial, i.e., moving from the cell center toward the cell boundaries.

4.2. Asymmetric Pi-Cell

Biaxial phenomena have been observed both experimentally and numerically in pi-cells with strong asymmetries [27,46]; in addition, the numerical experiments show that different OR mechanisms can cooperate to relax the nematic distortion, and such a phenomenon has been predicted for very strong distortions of the confined nematics induced by marked asymmetries combined with high enough intensities of applied electric pulses.

The application of asymmetric anchoring conditions to the pi-cell produces the propagation of asymmetric stress in the bulk of the NLC; hence, the growing of a biaxial region inside the cell in asymmetric position with respect the boundary plates can be expected, as depicted in Figure 2. The system investigated is constituted by the 5CB NLC [56,58–60], where a fixed pretilt angle on the lower boundary plate, $\theta_L = 19^\circ$, has been imposed, while on the upper plate, the pretilt angle $\theta_U \in [0, -1^\circ, -2^\circ, -3^\circ]$ has been imposed. In a first approach, the electric pulse amplitude ranged from $E = 10$ V/μm to $E = 14$ V/μm with step $\Delta E = 1$ V/μm, having verified that imposing symmetric anchoring conditions with $\theta_{L/U} = +/-19^\circ$, the electric pulse amplitude threshold for the OR is $Eth = 8$ V/μm [56]. It has been seen that with symmetric anchoring conditions, the biaxial OR occurs always in the center of the cell, the speed of which increases not only with increasing the intensity of the applied electric pulse, but also with increasing pretilt angles compared to the planar condition, see Table 1. In the case of the asymmetric pi-cell, it emerges that, with a proper combination of electric and mechanical stresses, the biaxial wall, ending with the OR that relaxes the large, induced distortion, can be moved both in time and space. Furthermore, a surface OR (SOR) can occur in the region close to the boundary plate where the nematic molecules approach planar pretilt angles. Table 2 summarizes the temporal position $\Delta\tau$ of the bulk OR (BOR) as a function of both the upper pretilt angle and the intensity of the applied electric pulse: the last column refers to the position δH of the BOR along the cell thickness measured from the upper plate, while the SOR occurs close to the upper boundary plate. It follows that, whatever the intensity of the applied electric pulse is, for $\theta_U = -3^\circ$, a BOR occurs always in the bulk located about 0.05 μm below the upper boundary plate, with increasing speed going from $E = 10$ V/μm to $E = 14$. The increase in the nematic stress at $\theta_U = -2^\circ$ causes the nematic distortion arising in the region to be relaxed, for $E = 13$ V/μm, by means of an SOR. At $E = 14$ V/μm, a BOR occurs about 0.03 μm below the upper boundary plate; instead for $\theta_U = -1^\circ$, only an SOR intervenes to relax the very strong distortion in the confined NLC. It must also be said that, once triggered, the SOR has a duration of several microseconds [56]. Even in this case, the MMPDE numerical technique allows us to monitor the biaxiality step by step, clearly distinguishing BOR from

SOR transitions, which is consistently supported by the computations of the electric current flowing across the cell, see again ref. [56].

Table 2. Summary of the temporal position $\Delta\tau$ of the BOR transition as a function of the upper pretilt angle and the intensity of the applied electric pulse, for $\theta_L = 19°$. The occurrence of the SOR in the upper boundary plate is indicated, whenever occurring. The spatial position δH of the BOR below the upper boundary plate is also indicated.

	E = 10 V/μm	E = 11 V/μm	E = 12 V/μm	E = 13 V/μm	E = 14 V/μm	
θ_U			$\Delta\tau$ (μs)			δH (μm)
0°	NT	NT	NT	NT	NT	//
−1°	NT	NT	NT	NT	SOR for $t \geq 58$	//
−2°	NT	NT	NT	SOR for $t \geq 85$	21	0.03
−3°	48	36	27	23	19	0.05

The computed maps of the biaxiality as a function of both pretilt angles and the amplitude of the applied electric pulse allowed us to lay the foundation for building a phase diagram of the OR transitions, extensively reported in refs. [58–60], by simulating the NLC behaviour under critical stress conditions to assess their switching properties regarding BOR and SOR. For such a purpose, massive computations, imposing pretilt angles on the upper boundary plate in the interval $19° \leq \theta_U \leq 0°$ with variable steps $\Delta\theta_U \in [0.1°, 1°]$, and intensities of the electric pulse in the range $15\ \text{V}/\mu\text{m} \leq E \leq 90\ \text{V}/\mu\text{m}$ with variable steps $\Delta E \in [1\ \text{V}/\mu\text{m}, 5\ \text{V}/\mu\text{m}]$, were performed, and for each computation, the switching mechanism relaxing the nematic distortion was deduced.

It results in the phase diagram in the (E, θ_U) plane [58,60] reproduced in Figure 3, which is parted in four regions where, depending on the combination of the mechanical and electrical stresses, the nematic texture can relax the distortion located close to the upper boundary plate (where the pretilt angle is smaller) by means of a BOR, then via a bulk switching (BS), or by means of an SOR, then via surface switching (SS). Moreover, a proper combination of the imposed stresses induces the relaxation by means of both BOR and SOR (BSS). Finally, the nematic texture may not undergo any switching (NS).

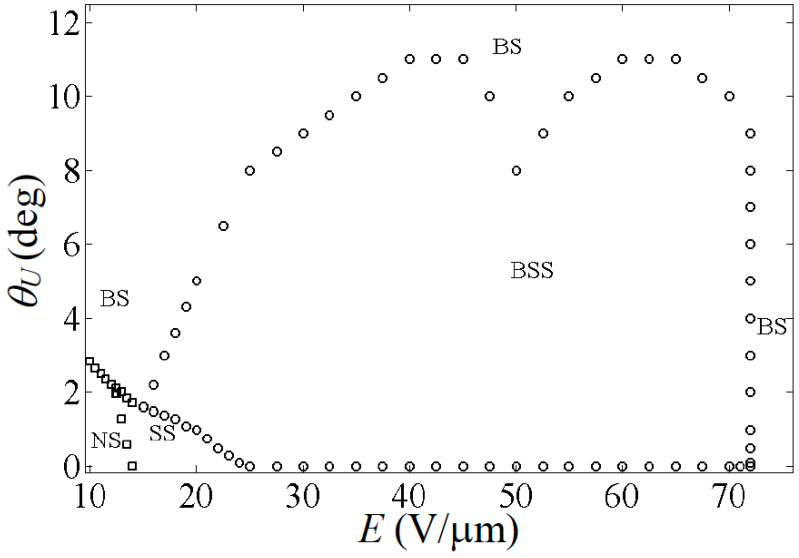

Figure 3. Phase diagram of the biaxial order reconstruction for $\theta_L = 19°$: on the horizontal axis is reported the amplitude of the applied electric pulse E, and on the vertical axis is reported the opposite of the anchoring angles θ_U. Squares and circles refer to numerical experiments presented in [56] and [58], respectively.

The phase diagram assumes a bilobed shape in a large region of the (E, θ_U) plane where the nematic texture relaxes the biaxial distortion by means of coexisting BOR and SOR. Monitoring the evolution of the eigenvalue of the $\boldsymbol{Q}$ tensor associated with the eigenvector parallel to the applied electric field indicates that, for textures falling in this region, two switching paths can be present which depend mainly on the intensity of the electric pulse [60]. In particular, a metastable uniaxial state can be superimposed on the SOR, the existence of which depends on the intensity of the applied electric pulse, and the duration of which depends on the pretilt angle imposed on the upper boundary plate; this is a result which potentially broadens the possibilities of exploiting the phenomenon for application purposes, but we are waiting for experimental studies that can confirm the theoretical predictions.

5. Conclusions and Future Work

The MMPDE adaptive technique is a powerful tool tailored for the numerical simulation of complex mathematical models of physical phenomena involving large-scale variations in time and space, and can be applied, in principle, to any differential problem discretizable in space. Indeed, it has recently been used to simulate complex biological systems as in refs. [78–83].

For NLCs confined in pi-cells, the application of mechanical and electrical stresses causes the growth of biaxial domains which relax the induced distortion. Above an appropriate threshold, which depends on both the intensity of the applied electric field and the pretilt angles for the nematic anchored to the boundary plates of the pi-cell, in the biaxial domains, an OR transition can originate. In-depth OR monitoring with the MMPDE technique gives predictions on the switching properties of the investigated nematic, suggesting that the OR may be controlled within the domain by fine tuning of the applied stresses. Moreover, the characterization of SOR and BOR opens the door to further exploitation of NLCs in the design and improvement of multi-stable optical devices. From a more fundamental point of view, the high-resolution computations allow us to distinguish first- and second-order transitions in the dynamics of the order tensor, identifying a metastable uniaxial state superimposed on a second-order transition, which is worthy of further theoretical and experimental investigations given its potential relevance for applicative purposes. In this direction, future research should be devoted to in-depth investigations, both theoretical and experimental, on the order of the phase transitions in two-dimensional and three-dimensional domains, then on the characterization of BOR and SOR, as well as on their mutual interaction in the induced relaxation of the biaxial stress. Moreover, the high spatial resolution which can be achieved by using the MMPDE technique could help to monitor coupling phenomena in electro-hydrodynamics of nematics due to viscosity effects, to distinguish anchoring breaking from order reconstruction phenomena, which is still an open issue [60]. On the other hand, the implementation of the MMPDE numerical technique in two-dimensional or even three-dimensional domains could provide new and more interesting insights into the dynamics of confined NLCs, helping to better characterize labile features, such as the metastable state discussed at the end of the previous section. A problem in extending MMPDE to higher spatial dimensions could arise from the required computing power, which in three spatial dimensions could lead to a prohibitive computational load. On the other hand, the method tested in [53] demonstrated the feasibility of the MMPDE in two spatial dimensions by applying it to the simulation of a defect inside a pi-cell. Other issues related to the extension of the MMPDE method to higher dimensional problems concern the choice of adaptive criteria and modelling with irregular geometries [51–53], and so far, there are no decisive applications to practical cases. These are some of the upcoming challenges that await the implementation of the MMPDE

numerical technique for NLCs modelling, towards which it is therefore desirable to direct future work.

Funding: This research received no external funding.

Institutional Review Board Statement: Not applicable.

Informed Consent Statement: Not applicable.

Data Availability Statement: Not applicable.

Acknowledgments: Work carried out in the context of the activities of the 'Gruppo Nazionale di Fisica Matematica (GNFM)' of the Italian 'Istituto Nazionale di Alta Matematica (INDAM) "Francesco Severi"'.

Conflicts of Interest: The authors declare no conflicts of interest.

References

1. Wang, W.; Zhang, L.; Zhang, P. Modelling and computation of liquid crystals. *Acta Numer.* **2021**, *30*, 765–851. [CrossRef]
2. Guardià, J.; Reina, J.A.; Giamberini, M.; Montané, X. An Up-to-Date Overview of Liquid Crystals and Liquid Crystal Polymers for Different Applications: A Review. *Polymers* **2024**, *16*, 2293. [CrossRef]
3. Andrienko, D. Introduction to liquid crystals. *J. Mol. Liq.* **2018**, *267*, 520–541. [CrossRef]
4. Sultanov, V.; Kavčič, A.; Kokkinakis, E.; Sebastián, N.; Chekhova, M.V.; Humar, M. Tunable entangled photon-pair generation in a liquid crystal. *Nature* **2024**, *631*, 294. [CrossRef] [PubMed]
5. Weima, S.A.M.; Norouzikudiani, R.; Baek, J.; Peixoto, J.A.; Slot, T.K.; Broer, D.J.; DeSimone, A.; Liu, D. Human interactive liquid crystal fiber arrays. *Sci. Adv.* **2024**, *10*, eadp0421. [CrossRef] [PubMed]
6. Barberi, R.; Ciuchi, F.; Durand, G.; Iovane, M.; Sikharulidze, D.; Sonnet, A.; Virga, E.G. Electric field induced order reconstruction in a nematic cell. *Eur. Phys. J. E* **2004**, *13*, 61–71. [CrossRef] [PubMed]
7. Boyd, G.D.; Cheng, J.; Ngo, P.D.T. Liquid-crystal orientational bistability and nematic storage effects. *Appl. Phys. Lett.* **1980**, *36*, 556–558. [CrossRef]
8. Amoddeo, A.; Barberi, R.; Lombardo, G. Moving mesh partial differential equations to describe nematic order dynamics. *Comput. Math. Appl.* **2020**, *60*, 2239–2252. [CrossRef]
9. Politano, G.G.; Filice, F.; Versace, C. Alignment of Nematic Liquid Crystal 5CB Using Graphene Oxide. *Crystals* **2023**, *13*, 1500. [CrossRef]
10. De Gennes, P.G.; Prost, J. *The Physics of Liquid Crystals*, 2nd ed.; Oxford University Press: New York, NY, USA, 1993.
11. De Gennes, P.G. Phenomenology of short-range-order effects in the isotropic phase of nematic materials. *Phys. Lett. A* **1969**, *30*, 454–455. [CrossRef]
12. Oseen, C.W. The theory of liquid crystals. *Trans. Faraday Soc.* **1933**, *29*, 883–899. [CrossRef]
13. Franck, F.I. Liquid crystals. On the theory of liquid crystals. *Discuss. Faraday Soc.* **1958**, *25*, 19–28. [CrossRef]
14. Biscari, P.; Cesana, P. Ordering effects in electric splay Freedericksz transitions. *Contin. Mech. Thermodyn.* **2007**, *19*, 285–298. [CrossRef]
15. Demus, D.; Goodby, J.; Gray, G.W.; Spiess, H.-W.; Vill, V. *Physical Properties of Liquid Crystals*; Wiley-VCH: Weinheim, Germany, 1999.
16. Barberi, R.; Durand, G. Controlled textural bistability in nematic liquid crystals. In *Handbook of Liquid Crystals Research*; Collings, P.J., Patel, J.S., Eds.; Oxford University Press: New York, NY, USA, 1997; Chapter 15.
17. Schopohl, N.; Sluckin, T.J. Defect Core Structure in Nematic Liquid Crystals. *Phys. Rev. Lett.* **1987**, *59*, 2582–2584. [CrossRef] [PubMed]
18. Buscaglia, M.; Lombardo, G.; Cavalli, L.; Barberi, R.; Bellini, T. Elastic anisotropy at a glance: The optical signature of disclination lines. *Soft Matter* **2010**, *6*, 5434–5442. [CrossRef]
19. Kleman, M.; Lavrentovich, O.D. Topological point defects in nematic liquid crystals. *Philos. Mag.* **2006**, *86*, 4117–4137. [CrossRef]
20. Aliev, F.; Basu, S. Relaxation of director reorientations in nanoconfined liquid crystal: Dynamic light scattering investigation. *J. Non Cryst. Solids* **2006**, *352*, 4983–4987. [CrossRef]
21. Tjipto, E.; Cadwell, K.D.; Quinn, J.F.; Johnston, A.P.; Abbott, N.L.; Caruso, F. Tailoring the interfaces between nematic liquid crystal emulsions and aqueous phases via layer-by-layer assembly. *Nano Lett.* **2006**, *6*, 2243–2248. [CrossRef]
22. Yi, Y.; Lombardo, G.; Ashby, N.; Barberi, R.; Maclennan, J.E.; Clark, N.A. Topographic-pattern-induced homeotropic alignment of liquid crystals. *Phys. Rev. E* **2009**, *79*, 041701. [CrossRef]
23. Loudet, J.C.; Hanusse, P.; Poulin, P. Stokes Drag on a Sphere in a Nematic Liquid Crystal. *Science* **2004**, *306*, 1525. [CrossRef]

24. Smalyukh, I.I.; Lavrentovich, O.D.; Kuzmin, A.N.; Kachynski, A.V.; Prasad, P.N. Elasticity-Mediated Self-Organization and Colloidal Interactions of Solid Spheres with Tangential Anchoring in a Nematic Liquid Crystal. *Phys. Rev. Lett.* **2005**, *95*, 157801. [CrossRef] [PubMed]
25. Musevic, I.; Skarabot, M.; Tkalec, U.; Ravnik, M.; Zumer, S. Two-dimensional nematic colloidal crystals self-assembled by topological defects. *Science* **2006**, *313*, 954–958. [CrossRef]
26. Qian, T. Biaxial ordering and field-induced configurational transition in nematic liquid crystals. *Liq. Cryst.* **1999**, *26*, 229–233. [CrossRef]
27. Ayeb, H.; Lombardo, G.; Ciuchi, F.; Hamdi, R.; Gharbi, A.; Durand, G.; Barberi, R. Surface order reconstruction in nematics. *Appl. Phys. Lett.* **2010**, *97*, 104104. [CrossRef]
28. Martinot-Lagarde, P.; Dreyfus-Lambez, H.; Dozov, I. Biaxial melting of the nematic order under a strong electric field. *Phys. Rev. E* **2003**, *67*, 051710. [CrossRef]
29. Ambrožic, M.; Kralj, S.; Virga, E.G. Defect-enhanced nematic surface order reconstruction. *Phys. Rev. E* **2007**, *75*, 031708. [CrossRef]
30. Biscari, P.; Napoli, G.; Turzi, S. Bulk and surface biaxiality in nematic liquid crystals. *Phys. Rev. E* **2006**, *74*, 031708. [CrossRef] [PubMed]
31. Klemencic, E.; Kurioz, P.; Kralj, S.; Repnik, R. Topological defect enabled formation of nematic domains. *Liq. Cryst.* **2020**, *47*, 618–625. [CrossRef]
32. Wu, J.; Ma, H.; Chen, S.; Zhou, X.; Zhang, Z. Study on concentric configuration of nematic liquid crystal droplet by Landau-de Gennes theory. *Liq. Cryst.* **2020**, *47*, 1698–1707. [CrossRef]
33. Barberi, R.; Ciuchi, F.; Lombardo, G.; Bartolino, R.; Durand, G.E. Time Resolved Experimental Analysis of the Electric Field Induced Biaxial Order Reconstruction in Nematics. *Phys. Rev. Lett.* **2004**, *93*, 137801. [CrossRef] [PubMed]
34. Joly, S.; Dozov, I.; Martinot-Lagarde, P. Comment on "Time Resolved Experimental Analysis of the Electric Field Induced Biaxial Order Reconstruction in Nematics". *Phys. Rev. Lett.* **2006**, *96*, 019801. [CrossRef]
35. Barberi, R.; Ciuchi, F.; Ayeb, H.; Lombardo, G.; Bartolino, R.; Durand, G.E. Reply to Comment on "Time Resolved Experimental Analysis of the Electric Field Induced Biaxial Order Reconstruction in Nematics". *Phys. Rev. Lett* **2006**, *96*, 019802. [CrossRef]
36. Ciuchi, F.; Ayeb, H.; Lombardo, G.; Barberi, R.; Durand, G.E. Control of transient biaxial order in calamitic nematics. *Appl. Phys. Lett.* **2007**, *91*, 244104. [CrossRef]
37. Ayeb, H.; Ciuchi, F.; Lombardo, G.; Barberi, R. Metallomesogens as biaxial dopants in a calamitic nematic liquid crystal. *Mol. Cryst. Liq. Cryst.* **2008**, *481*, 73–79. [CrossRef]
38. Lombardo, G.; Ayeb, H.; Ciuchi, F.; De Santo, M.P.; Barberi, R.; Bartolino, R.; Virga, E.G.; Durand, G.E. Inhomogeneous bulk nematic order reconstruction. *Phys. Rev. E* **2008**, *77*, 020702. [CrossRef] [PubMed]
39. Carbone, G.; Lombardo, G.; Barberi, R.; Musevic, I.; Tkalec, U. Mechanically Induced Biaxial Transition in a Nanoconfined Nematic Liquid Crystal with a Topological Defect. *Phys. Rev. Lett.* **2009**, *103*, 167801. [CrossRef] [PubMed]
40. Lombardo, G.; Ayeb, H.; Barberi, R. Dynamical numerical model for nematic order reconstruction. *Phys. Rev. E* **2008**, *77*, 051708. [CrossRef] [PubMed]
41. Pucci, G.; Lysenko, D.; Provenzano, C.; Reznikov, Y.; Cipparrone, G.; Barberi, R. Patterns of electro-convection in planar-periodic nematic cells. *Liq. Cryst.* **2016**, *43*, 216–221. [CrossRef]
42. Pucci, G.; Carbone, F.; Lombardo, G.; Versace, C.; Barberi, R. Topologically non-equivalent textures generated by the nematic electrohydrodynamic. *Liq. Cryst.* **2019**, *46*, 649–654. [CrossRef]
43. Kralj, S.; Majumdar, A. Order reconstruction patterns in nematic liquid crystal wells. *Proc. R. Soc. A Math. Phys. Eng. Sci.* **2014**, *470*, 20140276. [CrossRef]
44. Zhou, X.; Zhang, Z.; Zhang, Q.; Ye, W. Order Reconstruction in a Nanoconfined Nematic Liquid Crystal between Two Coaxial Cylinders. *Materials* **2015**, *8*, 8072–8086. [CrossRef]
45. Sun, Y.; Ye, W.; Zhang, Z. Order reconstruction in inverse twisted nematic cell with an applied electric field. *Phys. Lett. A* **2016**, *380*, 1865–1871. [CrossRef]
46. Lombardo, G.; Amoddeo, A.; Ridha, H.; Ayeb, H.; Barberi, R. Biaxial surface order dynamics in calamitic nematics. *Eur. Phys. J. E* **2012**, *35*, 32. [CrossRef] [PubMed]
47. Zienkiewicz, O.C.; Taylor, R.L.; Zhu, J.Z. *The Finite Element Method*, 6th ed.; Butterworth-Heinemann: Oxford, UK, 2005.
48. Known, Y.W.; Bang, H. *The Finite Element Method Using Matlab*, 2nd ed.; CRC Press: Boca Raton, FL, USA, 2000.
49. Ramage, A.; Newton, C.J.P. Adaptive solution of a one-dimensional order reconstruction problem in Q-tensor theory of liquid crystals. *Liq. Cryst.* **2007**, *34*, 479–487. [CrossRef]
50. Ramage, A.; Newton, C.J.P. Adaptive grid methods for Q-tensor theory of liquid crystals: A one-dimensional feasibility study. *Mol. Cryst. Liq. Cryst.* **2008**, *480*, 160–181. [CrossRef]
51. MacDonald, C.S.; Mackenzie, J.A.; Ramage, A.; Newton, C.J.P. Robust adaptive computation of a one-dimensional Q-tensor model of nematic liquid crystals. *Comput. Math. Appl.* **2012**, *64*, 3627–3640. [CrossRef]

52. MacDonald, C.S.; Mackenzie, J.A.; Ramage, A.; Newton, C.J.P. Efficient moving mesh methods for Q-tensor models of nematic liquid crystals. *SIAM J. Sci. Comput.* **2015**, *37*, B215–B238. [CrossRef]
53. MacDonald, C.S.; Mackenzie, J.A.; Ramage, A. A moving mesh method for modelling defects in nematic liquid crystals. *J. Comput. Phys. X* **2020**, *8*, 100065. [CrossRef]
54. Amoddeo, A.; Lombardo, G.; Barberi, R. An advanced numerical method to describe order dynamics in nematics. In *AIP Conference Proceedings, Proceedings of the IUTAM-ISIMM Symposium on Mathematical Modeling and Physical Instances of Granular Flows, Reggio Calabria, Italy, 14–18 September 2009*; Goddard, J.D., Jenkins, J.T., Giovine, P., Eds.; American Institute of Physics: Huntington, NY, USA, 2010; Volume 1227.
55. Amoddeo, A.; Barberi, R.; Lombardo, G. Electric field-induced fast nematic order dynamics. *Liq. Cryst.* **2011**, *38*, 93–103. [CrossRef]
56. Amoddeo, A.; Barberi, R.; Lombardo, G. Surface and bulk contributions to nematic order reconstruction. *Phys. Rev. E* **2012**, *85*, 061705. [CrossRef]
57. Amoddeo, A.; Barberi, R.; Lombardo, G. Nematic order and phase transition dynamics under intense electric fields. *Liq. Cryst.* **2013**, *40*, 799–809. [CrossRef]
58. Amoddeo, A. Nematodynamics modelling under extreme mechanical and electric stresses. *J. Phys. Conf. Ser.* **2015**, *574*, 012102. [CrossRef]
59. Amoddeo, A. Concurrence of bulk and surface order reconstruction to the relaxation of frustrated nematics. *J. Phys. Conf. Ser.* **2016**, *738*, 012089. [CrossRef]
60. Amoddeo, A.; Barberi, R. Phase diagram and order reconstruction modeling for nematics in asymmetric π-cells. *Symmetry* **2021**, *13*, 2156. [CrossRef]
61. Mottram, N.J.; Newton, C.J.P. Introduction to Q-tensor theory. *arXiv* **2014**, arXiv:1409.3542.
62. Tang, T. Moving Mesh Methods for Computational Fluid Dynamics. *Contemp. Math.* **2005**, *383*, 141–173.
63. Haegland, B.; Skaflestad, B. *A Survey of Some Methods for Moving Grid and Grid Adaption*; Preprint numerics no. 2/2002; Norwegian University of Science and Technology: Trondheim, Norway, 2002.
64. Acikgoz, N.; Bottasso, C.L. Metric-driven mesh optimization using a local simulated annealing algorithm. *Int. J. Numer. Methods Eng.* **2007**, *71*, 201–223. [CrossRef]
65. Barrett, J.W.; Feng, X.; Prohl, A. Convergence of a fully discrete finite element method for a degenerate parabolic system modelling nematic liquid crystals with variable degree of orientation. *Math. Model. Numer. Anal.* **2006**, *40*, 175–199. [CrossRef]
66. Patricio, P.; Tasinkevych, M.; Telo da Gama, M.M. Colloidal dipolar interactions in 2D smectic-C films. *Eur. Phys. J. E* **2002**, *7*, 117–122. [CrossRef]
67. James, R.; Willman, E.; Fernandez, F.A. Finite-Element Modeling of Liquid-Crystal Hydrodynamics with a Variable Degree of Order. *IEEE Trans. Electron. Devices* **2006**, *53*, 1575–1582. [CrossRef]
68. Mackenzie, J.A.; Mekwi, W.R. An hr-adaptive method for the cubic nonlinear Schrödinger equation. *J. Comput. Appl. Math.* **2020**, *364*, 112320. [CrossRef]
69. Huang, W.; Russel, R.D. *Adaptive Moving Mesh Methods*; Springer: New York, NY, USA, 2011.
70. De Boor, C. Good approximation by splines with variable knots. II. In Proceedings of the Conference on the Numerical Solution of Differential Equations, Dundee, Scotland, 3–6 July 1973; Watson, G.A., Ed.; Springer: Berlin/Heidelberg, Germany; New York, NY, USA, 1974; Volume 363, pp. 12–20. [CrossRef]
71. Pereyra, V.; Sewell, E.G. Mesh selection for discrete solution of boundary problems in ordinary differential equations. *Numer. Math.* **1974**, *23*, 261–268. [CrossRef]
72. Russell, R.D.; Christiansen, J. Adaptive mesh selection strategies for solving boundary value problems. *SIAM J. Numer. Anal.* **1978**, *15*, 59–80. [CrossRef]
73. White, A.B. On Selection of Equidistributing Meshes for Two-Point Boundary-Value Problems. *SIAM J. Numer. Anal.* **1979**, *16*, 472–502. [CrossRef]
74. Beckett, G.; Mackenzie, J.A.; Ramage, A.; Sloan, D.M. On The Numerical Solution of One-Dimensional PDEs Using Adaptive Methods Based on Equidistribution. *J. Comput. Phys.* **2001**, *167*, 372–392. [CrossRef]
75. Beckett, G.; Mackenzie, J.A. Convergence analysis of finite difference approximations on equidistributed grids to a singularly perturbed boundary value problem. *Appl. Numer. Math.* **2000**, *35*, 87–109. [CrossRef]
76. Huang, W. Practical Aspects of Formulation and Solution of Moving Mesh Partial Differential Equations. *J. Comput. Phys.* **2001**, *171*, 753–775. [CrossRef]
77. Huang, W.; Ren, Y.; Russell, R.D. Moving Mesh Partial Differential Equations (MMPDES) Based on the Equidistribution Principle. *SIAM J. Numer. Anal.* **1994**, *31*, 709–730. [CrossRef]
78. Amoddeo, A. Adaptive grid modelling for cancer cells in the early stage of invasion. *Comput. Math. Appl.* **2015**, *69*, 610–619. [CrossRef]

79. Amoddeo, A. Moving mesh partial differential equations modelling to describe oxygen induced effects on avascular tumour growth. *Cogent Phys.* **2015**, *2*, 1050080. [CrossRef]
80. Amoddeo, A. Oxygen induced effects on avascular tumour growth: A preliminary simulation using an adaptive grid algorithm. *J. Phys. Conf. Ser.* **2015**, *633*, 012088. [CrossRef]
81. Amoddeo, A. A moving mesh study for diffusion induced effects in avascular tumour growth. *Comput. Math. Appl.* **2018**, *75*, 2508–2519. [CrossRef]
82. Amoddeo, A. Modelling avascular tumor growth: Approach with an adaptive grid numerical technique. *J. Multiscale Model.* **2018**, *9*, 1840002. [CrossRef]
83. MacDonald, G.; Mackenzie, J.A.; Nolan, M.; Insall, R.H. A computational method for the coupled solution of reaction-diffusion equations on evolving domains and manifolds: Application to a model of cell migration and chemotaxis. *J. Comput. Phys.* **2016**, *309*, 207–226. [CrossRef] [PubMed]